

Quantum Diamonds at the Beach: Chemical Insights into Silica Growth on Nanoscale Diamond using Multimodal Characterization and Simulation

Perla J. Sandoval,[#] Karen Lopez,[#] Andres Arreola,[#] Anida Len, Nedah Basravi, Pomaikaimakalani Yamaguchi, Rina Kawamura, Camron X. Stokes, Cynthia Melendrez, Davida Simpson, Sang-Jun Lee, Charles James Titus, Virginia Altoe, Sami Sainio, Dennis Nordlund, Kent Irwin, and Abraham Wolcott*



Cite This: *ACS Nanosci. Au* 2023, 3, 462–474



Read Online

ACCESS |



Metrics & More



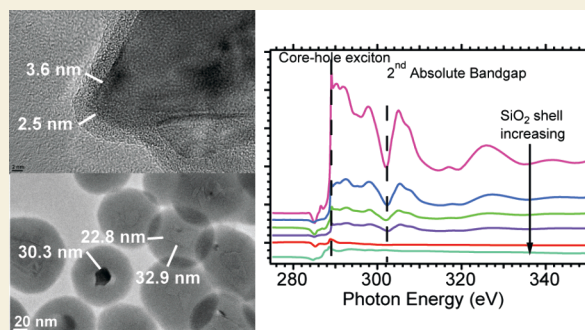
Article Recommendations



Supporting Information

ABSTRACT: Surface chemistry of materials that host quantum bits such as diamond is an important avenue of exploration as quantum computation and quantum sensing platforms mature. Interfacing diamond in general and nanoscale diamond (ND) in particular with silica is a potential route to integrate room temperature quantum bits into photonic devices, fiber optics, cells, or tissues with flexible functionalization chemistry. While silica growth on ND cores has been used successfully for quantum sensing and biolabeling, the surface mechanism to initiate growth was unknown. This report describes the surface chemistry responsible for silica bond formation on diamond and uses X-ray absorption spectroscopy (XAS) to probe the diamond surface chemistry and its electronic structure with increasing silica thickness. A modified Stöber (Cigler) method was used to synthesize 2–35 nm thick shells of SiO₂ onto carboxylic acid-rich ND cores. The diamond morphology, surface, and electronic structure were characterized by overlapping techniques including electron microscopy. Importantly, we discovered that SiO₂ growth on carboxylated NDs eliminates the presence of carboxylic acids and that basic ethanolic solutions convert the ND surface to an alcohol-rich surface prior to silica growth. The data supports a mechanism that alcohols on the ND surface generate silyl–ether (ND–O–Si–(OH)₃) bonds due to rehydroxylation by ammonium hydroxide in ethanol. The suppression of the diamond electronic structure as a function of SiO₂ thickness was observed for the first time, and a maximum probing depth of ~14 nm was calculated. XAS spectra based on the Auger electron escape depth was modeled using the NIST database for the Simulation of Electron Spectra for Surface Analysis (SESSA) to support our experimental results. Additionally, resonant inelastic X-ray scattering (RIXS) maps produced by the transition edge sensor reinforces the chemical analysis provided by XAS. Researchers using diamond or high-pressure high temperature (HPHT) NDs and other exotic materials (e.g., silicon carbide or cubic-boron nitride) for quantum sensing applications may exploit these results to design new layered or core–shell quantum sensors by forming covalent bonds via surface alcohol groups.

KEYWORDS: diamond, silica, nitrogen vacancy centers, core–shell nanoparticles, X-ray absorption spectroscopy



INTRODUCTION

Diamond has excellent physical and photophysical properties that are well suited for emergent applications in photonics,¹ quantum communication,^{2–5} quantum metrology,^{5–7} and biosensing.^{8–10} A unique combination of chemical inertness, a large optical band gap (5.5 eV), high thermal conductivity (25 W/cm•K), extreme hardness (10 on Mohs scale), and being the host of a library of color centers including the nitrogen-vacancy (NV) center makes diamond versatile in materials science. However, its all-carbon sp³ structure presents challenges in synthesizing uniform, covalently bound inorganic layers on diamond because of the high surface density of atoms (22 atoms/nm² on (110) and 18 atoms/nm² on (111)) and

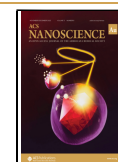
lattice mismatch. Epitaxial growth on diamond is notoriously difficult, and only SiC¹¹ and AlGaIn/GaN¹² layers have been successfully grown. Recently, Maurer and de Leon used nonepitaxial adhesion layers of Al₂O₃ on 100-terminated NVC diamond for quantum sensing of biological analytes, yet it was

Received: July 2, 2023

Revised: September 1, 2023

Accepted: September 6, 2023

Published: September 15, 2023



reported that the Al₂O₃ layer dissolved in buffer saline solutions at a rate of ~1 nm/day at 37 °C, reducing bound fluorescent dye counts by 50% over 1 week.¹³ To date, advancements in interfacing high-pressure, high-temperature (HPHT) nanoscale diamond (ND) with inorganic materials have been limited to amorphous SiO₂ or silica. Cigler and Wrachtrup used NV center ND with SiO₂ shells to decorate the diamond surface and engineer pH-selective chemistry for Gd sensing.¹⁴ Growth of SiO₂ shells on HPHT NDs is typically performed on “carboxylate-rich” NDs after an acid–base–acid treatment and has been shown to yield uniform layering across the ND surface.^{15–17} The uniform SiO₂ shell growth is a surprising result due to the limited number of carboxylates (~7% coverage) on the HPHT ND surface.¹⁸ One would expect SiO₂ islands if carboxylates were the functional group responsible for the nucleation and growth of SiO₂. The evidence presented here explains the mechanism, whereby silica chemistry is initiated by alcohols (silyl-ether bond formation) and highlights the use of synchrotron-based X-ray absorption spectroscopy (XAS) as an impactful tool in probing the core–shell nanostructure and surface termination. Support of our findings includes core-level X-ray detection using the transition edge sensor (TES) to generate a full electronic map of occupied and unoccupied electronic states.

Synchrotron-based XAS has been versatile in investigating the electronic structure, coordination state, and bond distance of mixed material systems. In combination with electron microscopy and elemental analysis, XAS provides fundamental information about complex systems used in biolabeling, energy, and catalysis applications. Core–shell nanostructures are ubiquitous in the fields of materials chemistry, physics, and engineering, with CdSe/ZnS quantum dots (QDs) being the most investigated along with a catalogue of other core–shell structures.^{19–21} XAS studies with CdSe/ZnS QDs have included ligand exchange chemistry,²² exciton binding energy measurements,²³ and CdSe/ZnS electronic structure studies with elucidation of the ZnS shell oxidation states.²⁴ Magnetic Fe/Fe₂O₃ nanoparticles (NPs) examined with XAS revealed the iron and iron oxide bonding environment while also detecting trace boron and nickel used during the synthetic protocol.²⁵ An XAS investigation of Fe/Ag and Ag/Fe core–shell NPs produced by a sodium borohydride reduction of Ag and Fe salts was able to discern subtle FeB and Fe₂B surface bonding environments.²⁶ Other materials studies of Ni/Au,²⁷ Fe/Fe_xO_y,²⁸ Pt–Ru,²⁹ Co–Pt,³⁰ Co–Au,³¹ and Cu–Ru³² all provided deeper insights into the chemical bonding with near-edge and extended X-ray spectroscopies. In contrast, this study is the first XAS examination of HPHT NDs with silica shells (ND–SiO₂). Silica chemistry on HPHT NDs has been the sole shell material demonstrated to date that bonds directly to the diamond core.^{14,16,33,34} The ND–SiO₂ system is unique because of the known difficulties in epitaxial growth on diamond, the fingerprint electronic structure of diamond, and this study confirms that XAS characterization of diamond core–shell nanostructures is possible.

C 1s XAS is widely used to probe graphene and other allotropes of carbon including diamond and diamond-like materials and can detect trace dopants in those materials.^{35–37} Diamond has a distinct electronic structure, and the first observation of the diamond core-hole exciton led to the determination of its binding energy (BE) of 0.19 eV, in good agreement with the calculated BE using the effective-mass approximation.³⁸ The diamond electronic structure can be

tracked using the distinct core-hole exciton features at 289.0 eV and the second absolute band gap at ~302 eV present in HPHT NDs.³⁹ While many layered materials and core–shell nanomaterials exist and are essential for energy, medicine, and defense, this study establishes a baseline for examining diamond–metal oxide nanostructures with XAS.

The mechanisms for detection of the diamond electronic structure in this study are based on the total electron yield (TEY) photocurrent and the effective escape depth L . Core level C 1s transitions will occur when a soft X-ray is absorbed, causing the electron to transition to an unoccupied electronic state that contains contributions from p-orbitals and is electric-dipole-allowed ($L = \pm 1$). The X-ray absorption event creates a core-hole in the material, and several well-understood mechanisms generate the TEY photocurrent. The contributions to the TEY photocurrent include low-energy electrons that have escaped the sample surface through three mechanisms: escape of primary photoelectrons, Auger electrons, and secondary inelastic Auger electrons, each with their own distinct kinetic energies, probe depths, and surface sensitivities. The main source of TEY photocurrent is due to inelastic electron–electron scattering of the Auger electrons and are of low energy ($K_e < 250$ eV).^{40–42} The effective escape depth, L , is similar to the electron mean free path of electrons and is a function of material type and the electron's kinetic energy. In metals and semiconductors, L is typically less than 5 nm, and insulators tend to have a larger L ; Al₂O₃ has L as large as 13 nm.⁴³ Diamond being an insulator with a 5.5 eV band gap should have L within the range of other insulators such as Al₂O₃. The escape depth L is provided within the description of the TEY photocurrent as described by Stöhr as

$$I(z) = \frac{\Omega}{4\pi} N_e e^{-z/L} h\nu M \quad (1)$$

where Ω is the collection angle, N_e is the number of emitted electrons, z is the depth from the substrate surface, L is the effective electron escape depth for the material, and $h\nu M$ is the gain function for the transport and escape of electrons into vacuum.⁴⁴

The exponential decay of the photocurrent, $e^{-z/L}$, has a similar exponential decaying profile of direct photoemission techniques such as X-ray photoelectron spectroscopy or XPS, with L being substituted for the inelastic mean free path λ . In contrast, L represents longer length scales than λ because the initial primary Auger electrons generate a cascade of much lower energy secondary electrons (<50 eV) with mean free paths longer than 10 nm. For example, TEY measurements of silicon with silicon oxide overlayers demonstrated sampling depths of ~5 and ~70 nm for the Si K-edge with 100 and 1840 eV electrons, respectively.⁴⁵ An in-depth simulation study of secondary inelastic Auger electrons by Ziaja and co-workers found 20–40 secondary Auger electrons were generated per primary Auger electron in the first 100 fs when using the Ashley and Tanuma-Powell-Penn model (TPP-2).⁴⁶ The cascade of secondary Auger electrons is the main source of electronic structure information in our XAS study, and the unique diamond signatures provide a fingerprint spectrum that cannot be confused with other types of carbon, such as adventitious carbon, graphite, and amorphous carbon.

Here, we demonstrate that the model system of HPHT NDs with the wet chemical growth of silica provides ample chemical control to extract fundamental aspects of the diamond TEY

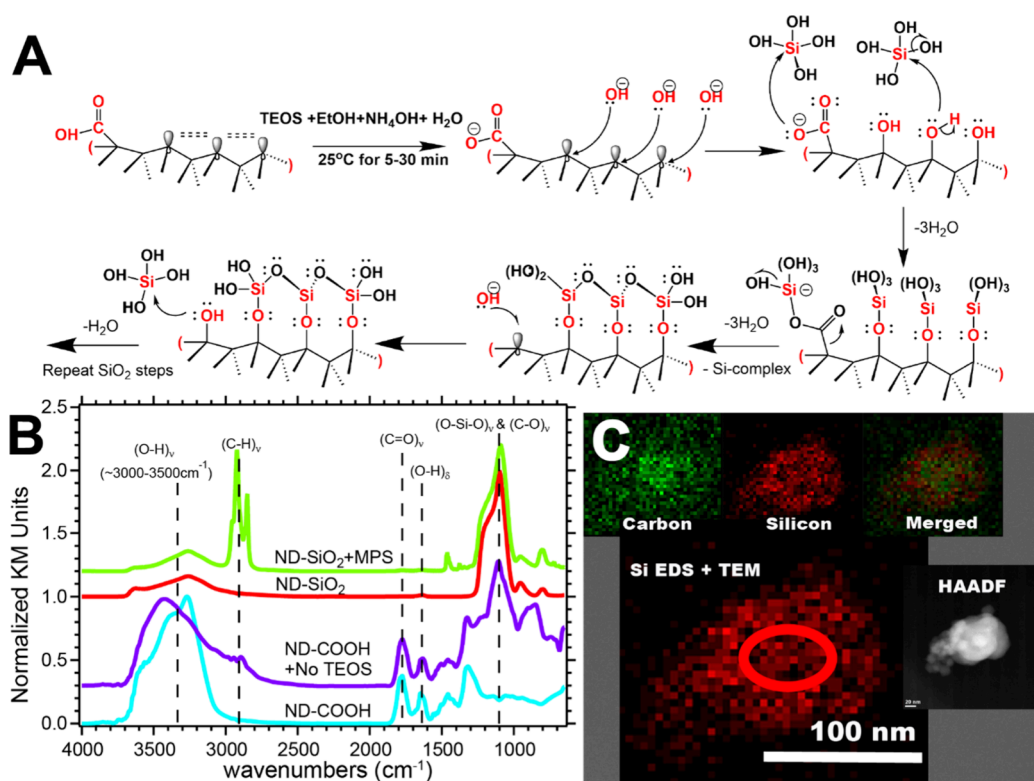


Figure 1. (A) Chemical scheme shows the growth of silica using tetraethyl orthosilicate in a base-catalyzed reaction similar to the Stöber method. The ND surface is depicted with 1 carboxylic acid and a sp^2 -like Pandey reconstruction. In the schematic, the alcohol groups after rehydroxylation are performing a nucleophilic attack to generate a silyl-ether bond on the diamond surface, and a subsequent removal of the acid occurs. (B) DRIFTS spectra of the ND constructs before and after silica shell growth show the reduction in the $(C=O)_\nu$ at 1785 cm^{-1} and the increase in $(Si-O-Si)_\nu$ at 1100 cm^{-1} . DRIFTS of the rehydroxylation control experiment is depicted and shows the increase of an alcohol peak at 1100 cm^{-1} . (C) A cluster of diamond nanoparticles encapsulated in silica is seen by electron microscopy. High-angle annular dark field (HAADF) microscopy is used to image the embedded diamond in silica, while elemental mapping of $C\ K\alpha$ and $Si\ K\alpha$ EDS is used to spatially resolve the core-shell structure.

signal, the growth mechanism of the silica itself, and chemical analysis. Carboxylate-rich HPHT NDs, produced by an acid–base–acid (ABA) treatment of alcohol-rich NDs, were reacted with silica precursors in solution using a modified Stöber method as described by Cigler and colleagues.⁴⁷ This study reveals that ethanol with ammonium hydroxide solutions used for silica growth adds alcohols to the ND surface (rehydroxylation) prior to silica growth and these alcohols are responsible for the silica growth via silyl-ether bond formation ($C-O-Si$). Conformation of the covalent attachment of the silica to the diamond surface was tested with thermogravimetric analysis-mass spectroscopy (TGA-MS) and showed no desorption of silanes or silicon-based precursors (see S2). Silane-based functionalization of the $ND-SiO_2$ samples with polyethylene glycol, amines, azides, carboxylic acids, glycidyls, and fluorines was probed via XAS to demonstrate the chemical versatility of the silica surface. The correlation between high-resolution transmission electron microscopy (HRTEM) imaging and $C\ 1s$ XAS data shows that all diamond features are fully suppressed within an $\sim 20\text{ nm}$ thick SiO_2 shell on the ND core. The effective electron escape depth (L) was calculated to be $\sim 14\text{ nm}$ based on our analysis of the $C\ 1s$ signal coming exclusively from the diamond core–hole exciton. These results are consistent with the TEY signal originating from inelastically scattered secondary Auger electrons (electron cascade). Modeling of the $CKL1L1$ (246.8 eV), $CKL1L23$ (257.4 eV), and $CKL23L23$ (268.0 eV) Auger electrons and the number of secondary collisions using the NIST SESSA

program reinforces our results (see S1). Our findings elucidate the mechanism of covalent diamond-silica growth and should inspire new core-shell architectures to be explored for quantum sensing and biolabeling with quantum bits such as the nitrogen vacancy center in diamond and other alcohol-terminated exotic materials.

RESULTS AND DISCUSSION

Surface Rehydroxylation and Silyl Ether Bond Formation on Diamond

The growth of amorphous silica on carboxylate-rich HPHT NDs ($ND-COOH$) was found to proceed with alcohols on the diamond surface and led to decarboxylation. Silica growth is performed with ethanol, ammonium hydroxide, water, tetraethyl orthosilicate (TEOS), and $ND-COOH$ in a similar fashion to SiO_2 nanoparticle synthesis. Hydroxylation was confirmed in a simple control experiment without TEOS in basic ethanol and showed a definitive increase in $(C-O)_\nu$ at 1100 cm^{-1} representative of an alcohol-rich diamond. The proposed mechanism for covalent bond formation on the oxidized surface of HPHT NDs is detailed in Figure 1 and shows the conversion from carboxylates to alcohols and subsequent silica chemistry. We found that rehydroxylation did not cause the loss of carboxylates but instead occurred after silica bond formation. TEOS is the sole silicon precursor for the formation of SiO_2 , and its hydrolysis is known to be base-catalyzed via nucleophilic attack of the Si atom.⁴⁸ We use mildly basic conditions ($pH \sim 11$) with NH_4OH to control the

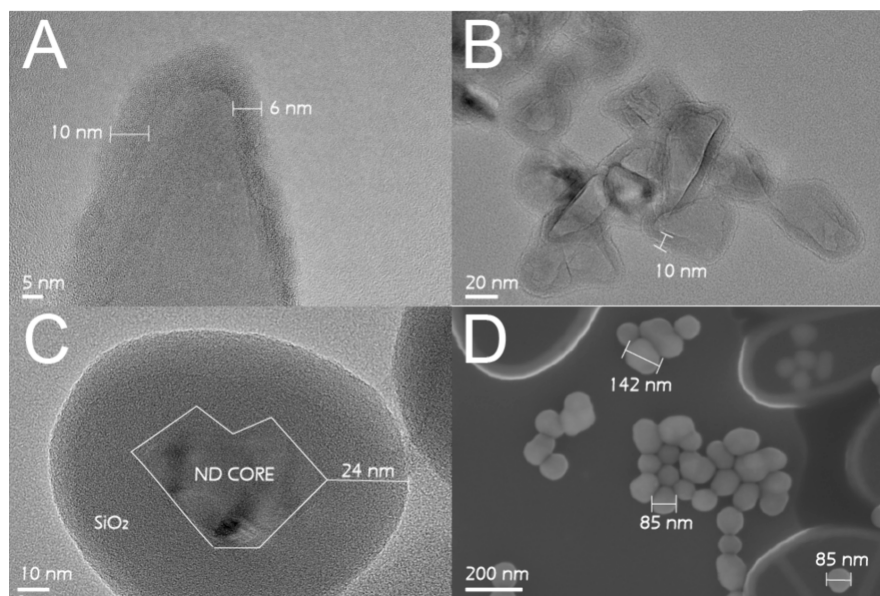


Figure 2. Thickness of silica on the HPHT ND cores is controlled by the length of the reaction time and increased growth forms nearly spherical ND-SiO₂ at approximately 20 nm thickness. High-resolution TEM imaging shows ultrathin SiO₂ growth surrounding an irregular nanodiamond core with measurements of 6–10 nm around the ND edge and basal plane (A). Ten nanometer SiO₂ growth is depicted on an aggregate of nanodiamonds of varying diameters and morphologies (B). With increasing reaction time of 20 min, 20–25 nm shells can be synthesized and the ND-SiO₂ is generally spherical. (C) High-resolution SEM image shows multiple particles in a cluster and the size distribution is demonstrated with a 85 and 142 nm being highlighted (D).

kinetic rate of TEOS hydrolysis and silica growth on the ND surface. Previously discussed mechanisms for hydrolysis and polymerization include both penta- and hexacoordinate intermediates, leading to the formation of silicates and SiO₂ particles.^{49–51} With HPHT NDs, the nucleophilic attack by alcohols (C–O–H) or alkoxide groups (C–O[−]) on the ND surface occurs to form the ND–Si(OH)₄ intermediate and the elimination of H₂O. In a classic Stöber method, the condensation reaction would form SiO₂ clusters that nucleate and form submicron particles.⁵² In this route we call the Cigler method, bond formation on the ND surface undergoes further –O–Si–O– polymerization reactions to produce a SiO₂ shell of the desired thickness.

Silica shell growth was tracked with diffuse reflectance infrared Fourier transmission spectroscopy (DRIFTS), which was confirmed with transmission electron microscopy (TEM) and energy dispersive X-ray spectroscopy (EDS). DRIFTS data in Figure 1B show surface chemistry of the ND–COOH before and after silica chemistry, and distinct vibrational features can be observed. The carboxylated ND sample (ND–COOH) produced from the ABA protocol shows a distinct (C=O)_v peak at 1780 cm^{−1} and no peak at 1100 cm^{−1}. Synthesis of the SiO₂ shells eliminates the (C=O)_v feature and the vibrational feature is no longer observed at 1780 cm^{−1}. A control experiment was designed whereby ND–COOH, ammonium hydroxide, water, and ethanol without the silica precursor were prepared and reacted in the same conditions as a standard synthesis (see SI methods). The resulting DRIFTS spectrum clearly shows the increase in (C–O)_v peak at 1100 cm^{−1} representative of alcohols. The increase in alcohols is thought to occur through the addition of hydroxides (OH[−]) across the Pandey chain reconstructed sp²-like ND surface and is illustrated by dashed lines in the proposed mechanism.⁵³ After SiO₂ growth on the ND cores, the peak at 1780 cm^{−1} is no longer present due to the desorption of a silicate complex

from the surface. After SiO₂ growth, a prominent (O–Si–O)_v peak arises at 1100 cm^{−1} with a distinct line shape in comparison with the original alcohol termination. EDS mapping of C Kα, O Kα (not shown), and Si Kα signals was performed across an ND cluster with a 20+ nm silica shell, and a correlation of increased C Kα intensity from the ND core can be observed in Figure 1C. Si Kα signals are observed throughout the sample and consistent with the nanoparticle morphology imaged with high-angle annular dark field microscopy. The imaged ND–SiO₂ cluster represents a nonuniform coating of the SiO₂, which can occur when the growth conditions are nonoptimal. In a demonstration of SiO₂ surface chemistry, mercaptopropyl trimethoxysilane is used to generate outward-facing sulfhydryl groups (–SH) and (C–H)_v features arising from the propyl chain at 2800–2900 cm^{−1} can be clearly observed. Amines and poly(ethylene glycol) chains can also be grafted to the ND–SiO₂ constructs and were used to stain neuronal cells in an NV center fluorescence demonstration (see S2).

Time-Dependent Silica Growth on HPHT ND Cores and Suppression of the Diamond Electronic Structure

High-resolution transmission electron and scanning electron microscopy confirmed the thickness and distribution of the SiO₂ across the NDs and were used quantitatively to understand the suppression of the diamond electronic structure observed in XAS. The shell thickness was controlled by the length of the reaction as detailed in the Methods section. Representative images with scale bars are shown in Figure 2 and clearly illustrate the transition from the ND core and the amorphous SiO₂ shell. The irregularly shaped ND crystallites generated through a ball milling process have edges and facets that are followed closely by the 6–10 nm SiO₂ shell on the tip of an ND, as shown in Figure 2A. A collection of NDs of various sizes and shapes is also shown in Figure 2B and allows a clear contrast between the diamond core and the

nanometer-thick SiO₂ shells. As the SiO₂ shell increases in thickness, the ND morphology transitions from irregular to spherical as previously discussed by Chu¹⁷ and can be observed with a 20+ nm shell in panel 2C. The ND is outlined in white to clearly depict the ND–SiO₂ transition and to quantify the shell thickness. Dynamic light scattering was also used to confirm the purification steps, solubility, and aggregation state (data not shown). Additional TEM images show the morphology and range of shell thicknesses on the HPHT ND cores (S4 and S5) and XPS analysis of 5 nm shells reveals the 4× reduction in the C 1s signal and the stoichiometry of the SiO₂ overlayer (S6).

Suppression of the diamond electronic structure was unambiguously observed as a function of SiO₂ shell thickness, and the diamond TEY yield signal is dominated by inelastic Auger electrons that travel from the diamond through the amorphous silica shell. The HPHT ND electronic structure is the same as single crystal bulk diamond and includes the diamond core-hole exciton and second absolute band gap at 289.0 and 302 eV, respectively.³⁸ The C 1s XAS data is collected at beamlines 8–2 and 10–1 at the Stanford Synchrotron Radiation Lightsource (SSRL), and the experimental setup is detailed in the SI methods section. Raw XAS data are interpolated, and linear background subtraction is performed in the pre-edge region from 270 to 280 eV. The TEY signal is normalized to the beam current I_0 and is energy calibrated to the diamond core–hole exciton at 289.0 eV (Figure 3A). The position of the core–hole exciton and second absolute band gap does not change with overlayer thickness and can be observed clearly with 0–15 nm silica shells (traces A through D). Trace E in Figure 3B with a 20 ± 5 nm shell no longer has an observable core-hole exciton peak, and a minor dip for the second absolute band gap is observed and represents a diminished diamond signal. The presence of a second absolute band gap feature, yet lacking the core-hole exciton is commonly observed with C 1s XAS of detonation NDs and indicative of the diamond electronic structure.⁵⁴ Trace F has no observable diamond features, and the C 1s signal originated from adventitious carbon on the ND–SiO₂ surface. The core-hole exciton signal divided by the pre-edge background (TEY/BKGD) is plotted in Figure 3C and the natural log of TEY/BKGD was fit with a linear least-squares regression (Figure 3C inset), and the slope value was then used to produce the exponential decay fit in Figure 3C. The TEY/BKGD signal follows an exponentially decaying profile as described in eq 1 and based on the exponential fit shows a 95% decrease in TEY/BKGD signal at ~14 nm of SiO₂ thickness and a 99.9% decrease with ~35 nm SiO₂ shell thickness. Frazer et al. evaluated a 0.1% TEY/BKGD signal as the maximum probing depth (MPT) with metal films.⁵⁵ The maximum probing depth or MPD based on a 0.1% TEY/BKGD in this study shows no signatures of the diamond core-hole exciton, and therefore, an MPD of 35 nm is not justified in this study. Therefore, we conclude that diamond electronic signatures can be discerned up to ~15 nm of SiO₂ thickness.

Modeling of the C 1s Auger electrons and their intensity as a function of SiO₂ overlayer thickness qualitatively agree with our observations. The NIST SESSA program was used to simulate the behavior of primary Auger electrons and inelastic secondary electrons.⁵⁶ The simulation focused on the diamond core-hole exciton, which we used for our analysis, the photon energy of 289.0 eV used for excitation, and the three CKL Auger electrons that are generated (see the SI for SESSA

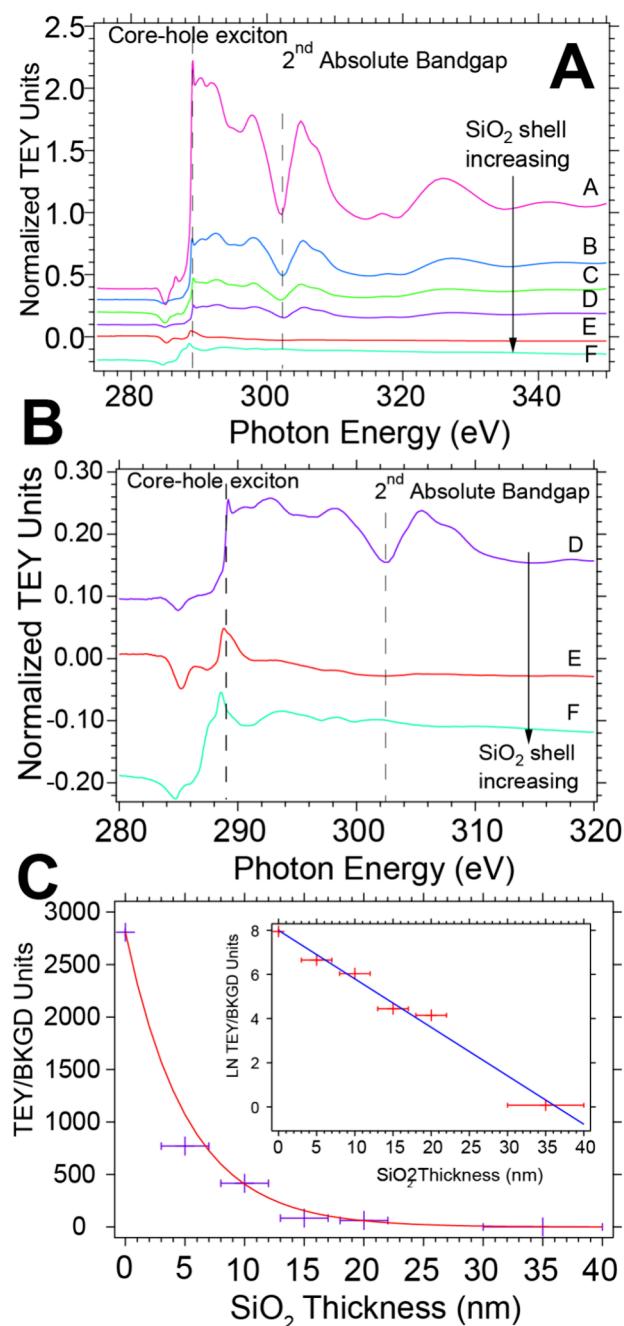


Figure 3. XAS spectra was found to effectively track the growth of silica via the decrease in diamond electronic structure and decreased exponentially due to inelastic Auger electrons generating the sample current. The distinct diamond structure decreases in signal intensity with increasing silica shell as the core-hole exciton and 2nd absolute band gap decrease (A). Plots D, E, and F are C 1s XAS of ND–SiO₂ samples with 13 ± 5, 20 ± 5, and 35 ± 5 nm silica shells, respectively, where the diamond core-hole features are diminished or eliminated (B). The diamond core-hole intensity (TEY/BKGD) versus SiO₂ thickness shows an exponential decrease, while the inset shows the natural logarithm of the TEY/BKGD signal with a linear least-squares regression and the resultant rate was used to generate the exponential fit of the raw TEY/BKGD data (C).

details). Forty inelastic collisions are modeled, similar to the 20–40 inelastic collisions in the first 100 fs of Ziaja et al.⁴⁶ Figure 4 summarizes the electron spectra of a 30 nm diamond core–shell nanoparticle with varying SiO₂ shell thickness from

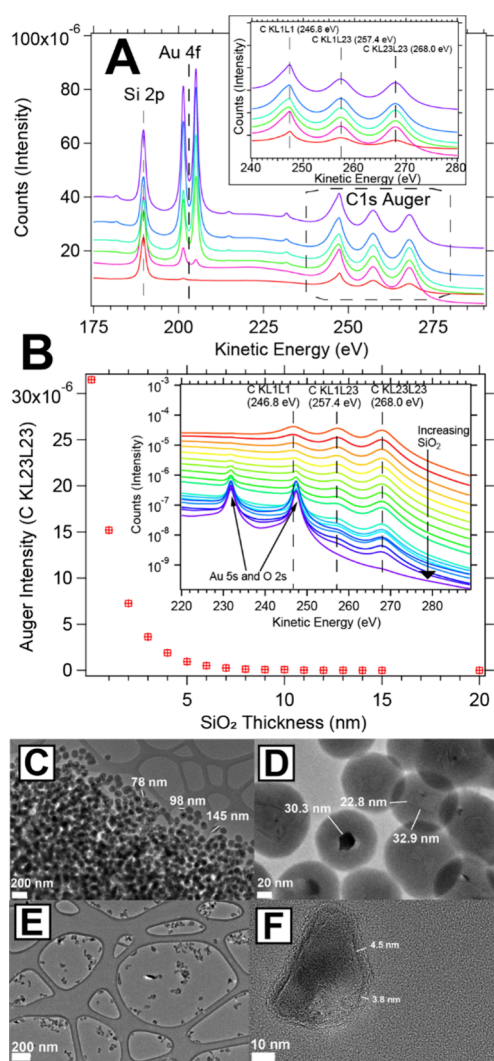


Figure 4. SESSA simulations qualitatively supported the experimental TEY data of ND–SiO₂ samples with increasing shell thickness (A) SESSA-based electron spectra for 30 nm diamond with 0.1–20 nm thick SiO₂ shell. The top spectrum is representative of a 30 nm diamond with a 5 nm thick shell and reveals the signals from the gold substrate, SiO₂ shells, and diamond core with detector angles from 0 to 75° in 15° increments. The inset shows the 3 Auger CKL features from 245 to 268 eV for a 5 nm thick SiO₂ shell. A plot of the C KL23L23 intensity versus shell thickness shows an exponential decay consistent with our C 1s XAS data. The inset of the middle panel are simulations with a detector angle of 55°, an energy range of 220–290 eV and increasing SiO₂ shell thickness from 0.1 to 20 nm. (B) TEM images of thick (20–30 nm) and thin (<5 nm) silica shells on HPHT ND cores are for reference to the Auger simulations generated by SESSA (C–F).

0.1 to 20 nm on a gold substrate. Simulated electron spectra of a 5 nm SiO₂ shell at varying detector angles are presented in Figure 4A, and the inset shows the Auger electrons for C KL1L1, C KL1L23, and C KL23L23 at 246.8, 257.4, and 268.0 eV, respectively. A 55° detector angle was used to simulate Auger electron spectra in the kinetic energy range 220–290 eV (see inset of Figure 4B). The C KL23L23 Auger intensity showed an exponential decay with respect to SiO₂ shell thickness, in agreement with the experimental C 1s XAS signal in TEY mode. The C KL23L23 feature was completely suppressed with a 20 nm shell. TEM images of NDs with silica

shells of 20–30 nm and <5 nm are shown to illustrate the actual distribution of ND core sizes and silica shell thicknesses in this study in Figure 4C. Overall, the simulations with SESSA are in good agreement with the C 1s XAS spectra, the supporting TEM images, and show that primary Auger electrons produced from 289.0 eV photons at the diamond core-hole exciton yield an inelastic electron cascade that probes ~15 nm into the core–shell nanoarchitecture.

XAS Conformation of Decarboxylation during SiO₂ Growth, Different Carboxylate-Diamond versus Molecular Carboxylate XAS Signatures, and Silane-Mediated Molecular Decoration

Amorphous silica is a wide band gap insulator (~9 eV) and causes the removal of acids on the HPHT ND surface while providing a flexible platform for chemical functionalization with amines, amides, azides, carboxylates, and fluorines. O 1s XAS data from the 1s XAS reveal distinct features supporting the conclusion that carboxylates are removed during silica growth and that diamond surface carboxylates are distinct from molecular carboxylates from silane-based chemistry. O 1s spectra in panel A show no $\pi^*(C=O)$ transition and a strong $\sigma^*(C-O)$ for ND–OH as expected for alcohol-rich diamond, and a $\pi^*(C=O)$ peak does emerge for ND–COOH at 530.2 eV after ABA chemistry is used (see the SI for methods).^{39,57} After silica shell growth, the ND–SiO₂ constructs show no $\pi^*(C=O)$ transitions at 530.2 eV reinforcing that silica growth causes decarboxylation. The mechanism for the loss of carboxylates with Si(OH)₄ under basic ethanolic conditions is beyond the scope of this work, yet the bonding of SiO₂ and CO₂ under high-pressure and high-temperature conditions has been reported.⁵⁸ Santoro et al. described uni-, bidentate-, and bridged bonding of silicon carbonates and can provide a chemical framework for our observed decarboxylation when ND–COOH → ND–SiO₂. After molecular decoration of ND–SiO₂ with carboxyethylsilanetriol sodium salt, a new $\pi^*(C=O)$ peak is observed at 532.2 eV representing a molecular carboxylate, a +2 eV shift from carboxylates bound to the diamond surface. Previous O 1s XAS studies by Outka and Stöhr of formic and propanoic acid bound to Si (111) surfaces show similar $\pi^*(C=O)$ peak positions at 532.8 eV.⁵⁷ In comparison, glycidyl molecular decoration (ND–SiO₂ + Gly), with a strained epoxy ring, contained a $\sigma^*(C-O)$ and $\sigma^*(Si-O)$ shape resonance ranging from 535 to 540 eV, and the XAS of the O 1s largely mimics the ND–SiO₂ spectrum. ND–SiO₂ + Gly also contains two small peaks at 529.0 and 531.5 eV caused by X-ray beam damage⁵⁹ that formed $\pi^*(C=O)$ electronic states through a loss of protons, as the starting glycidyl contains only single C–O bonds.

Molecular functionalization with polyethylene glycol (PEG), amines, and azides is used for biolabeling protocols and click chemistry and was confirmed with N 1s XAS. PEG and amines are important stabilizing and linking groups for biolabeling and biosensing with NV centers.¹⁴ Neuronal biolabeling with ND–SiO₂ + PEG + NH₃ containing NV centers is shown in Figure S3 and clearly demonstrates the ability to use NV center fluorescence to distinguish the axon, axon hillock, and dendrites in neurons. Linking chemistry with amines is common with sulfo-NHS/EDC coupling, and azides are widely used in click chemistry. First, we modify the amine content and examine the use of N 1s XAS for ND–SiO₂ + PEG + NH₃ with PEG–amine ratios of 10:1 and 4:1, showing an increased N 1s signal with the 4:1 ratio sample. Peaks at

400.9 and 405.1 eV are assigned to $\sigma^*(\text{N-H})$ and $\sigma^*(\text{N-C})$ transitions, respectively (Figure 5B). X-ray damage of the aminated ND sample causes a weak $\pi^*(\text{C=N})$ transition to arise at 398.3 eV and has been reported previously by Leinweber et al.⁵⁹ Aminated ND-SiO₂ was then conjugated to folic acid using sulfo-NHS/EDC and resulted in a strong $\pi^*(\text{C=N})$ peak arising at 398.0 eV due to amides present in the folate molecules and the new amide bonds that were formed on the ND-SiO₂ + PEG + NH₃ surface. From our N 1s XAS study, the chemically versatile amine group can be followed from its initial state, X-ray damage side products, and bioconjugated final state after using sulfo-NHS/EDC coupling reactions. Aminated ND-SiO₂ samples were also probed with the transition edge sensor at beamline 10-1, and C 1s, N 1s, and O 1s occupied and unoccupied states were extracted from resonant inelastic X-ray scattering (RIXS) maps as previously described with direct diamond-amine bond formation (see the SI).⁶⁰ The RIXS data and extracted partial fluorescence yield-XAS and X-ray emission spectroscopy (XES) data reinforce the chemical bonding assignments described here (see S7, S8, and S9 for C 1s, N 1s, and O 1s RIXS maps and spectra, respectively).

Azides produce a complex electronic spectrum of the linear $\text{N}=\text{N}^{\oplus}=\text{N}^{\ominus} \leftrightarrow \text{N}^{\ominus}-\text{N}^{\oplus}=\text{N}$ structure with six assigned peaks and shape resonances that are commonly exploited in click chemistry and is contrasted with a fluorine-decorated surface (Figure 5C). For clarity, the nitrogen atoms are denoted by N1, N2, and N3, where N1 is the terminal nitrogen of the azido moiety. N 1s peaks were observed at 398.5, 399.5, and 400.7 eV and were assigned to the triple and double bond resonance states of $\pi^*(\text{N1}\equiv\text{N}^{\oplus})$, $\pi^*(\text{N1}/3=\text{N}^{\oplus})$, and $\pi^*(\text{N2}=\text{N}^{\oplus})$, respectively. Shoulders and shape resonances at 403.1, 404.6, and 406.3 eV are assigned to the $\pi^*(\text{N2}=\text{N}^{\oplus})$, $\sigma^*(\text{N3-C})$, and $\sigma^*(\text{N}=\text{N})$ electronic states, respectively. The complexity of the azide structure has been clarified by density functional theory (DFT) calculations of the N 1s XAS spectrum.^{61,62} In two manuscripts, Darlatt reports two photon energies for the $\pi^*(\text{N1}\equiv\text{N}^{\oplus})$ transition at 398.6 and 399.6 eV. Our reported value of 398.5 eV is in agreement with their first report for a “pristine azide surface adsorbed monolayer”. In contrast, Darlatt’s second report did not agree with the first and reported the triple bond $\pi^*(\text{N1}\equiv\text{N}^{\oplus})$ and $\pi^*(\text{N1}/3=\text{N}^{\oplus})$ transitions were due to the 1s \rightarrow 2p resonance of the terminal N1 atom using DFT and cited values of 399.6 and 400.9 eV, respectively.⁶² The triple bond notation is used here to denote the contribution from sp hybridized orbitals in the $\text{N}^{\ominus}-\text{N}^{\oplus}=\text{N}$ resonance structure originally described by Pauling for methyl azide.⁶³ In contrast, a fluorinated ND-SiO₂-F sample was also produced using 3,3,3-trifluoropropyltrimethoxysilane and a strong F 1s TEY signal at 692.0 eV was assigned to the $\sigma^*(\text{C-F})$ resonance. The F 1s spectrum was similar to disordered PTFE films produced by a plasma deposition technique that generated primarily CF₃ functional groups.⁶⁴ Fluorinated HPHT NDs may be used for the preparation of hydrophobic NDs and ¹⁹F magnetic resonance imaging applications.^{65,66}

In conclusion, we have found that the growth of 2–35 nm SiO₂ shells on highly purified HPHT NDs can suppress the underlying electronic structure of the diamond core with a probing depth of ~15 nm. The silica growth mechanism was discovered to be driven by alcohols on the diamond surface, where hydroxylation occurs in basic ethanolic solutions and decarboxylation is prevalent during the silica growth reaction.

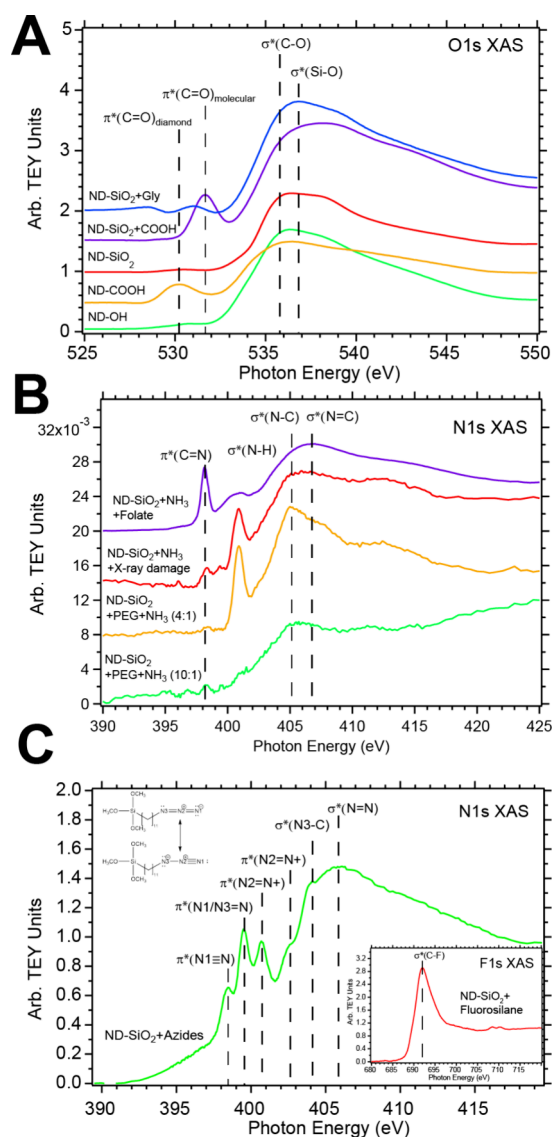


Figure 5. XAS spectra of ND-SiO₂ samples confirms the successful decoration of various molecules, the removal of carboxylate features after silica growth and differentiates between diamond bound versus molecular carboxylates. O 1s spectra of ND-OH, ND-COOH, ND-SiO₂, ND-SiO₂ + COOH, and ND-SiO₂ + glycidoxy (epoxide ring) are shown in the ascending order (A). Alcohol-rich ND-OH has only a $\sigma^*(\text{C-O})$ shape resonance at 536.4 eV, while ND-COOH (acid-base-acid treatment) has a $\pi^*(\text{C=O})$ transition at 530.2 eV that is assigned to carboxylates. ND-SiO₂ shows little $\pi^*(\text{C=O})$ signatures, while ND-SiO₂+COOH with folic acid functionalization chemistry has a distinct feature at 532.2 eV. ND-SiO₂-glycidoxy shows little $\pi^*(\text{C=O})$ and a shifted $\sigma^*(\text{C-O})$ transition at 537.3 eV for epoxides. N 1s XAS spectra of ND-SiO₂ + PEG + NH₂ (10:1 ratio), ND-SiO₂ + PEG + NH₂ (4:1 ratio), X-ray induced beam damage of the ND-SiO₂ + PEG + NH₂ with 4:1 ratio, and ND-SiO₂ + PEG + NH₂ + Folate provides conformation of amine functionalization and conjugation chemistry (B). N 1s XAS spectrum of ND-SiO₂ + azides is complex and shows resonance peaks for N1, N2, and N3 of the linear azide electronic structure. Peaks at 398.5, 399.5, 400.7, and 402.6 eV are assigned to $\pi^*(\text{N1}\equiv\text{N})$, $\pi^*(\text{N1}/3=\text{N})$, and two $\pi^*(\text{N2}=\text{N}^{\oplus})$ transitions, respectively. Shape resonances at 404.1 and 405.8 eV were assigned to $\sigma^*(\text{N3-C})$ and $\sigma^*(\text{N}=\text{N})$, respectively. In contrast, the inset shows the simple F 1s transition for $\sigma^*(\text{C-F})$ at 692.0 eV of a fluorinated ND-SiO₂ sample (C).

HRTEM and EDS were used to confirm the average SiO₂ shell thickness, and C 1s XAS data taken in TEY mode allowed the submerged diamond to be detected due to the inelastic secondary electron cascade produced by Auger electrons of 245–270 eV. XAS spectra of surface-functionalized ND–SiO₂ samples were collected for azide, amine, fluorine, and other surface moieties to demonstrate the chemical flexibility of the silica surface for biolabeling and biosensing applications using NV center NDs. Because the silica growth is uniform across the diamond surface due to abundant alcohol groups, this work should inspire new diamond–metal oxide core–shell nanostructures to be explored for quantum sensing and biolabeling applications.

■ EXPERIMENTAL METHODS AND PROCEDURES

Materials

HPHT ND powders were purchased from Microdiamant AG (monocrystalline diamond powder MSY 0–0.05 μm). Fluorescent HPHT NDs (5–30 nm) were provided by Bikanta, Inc. (Berkeley, CA), Adamas Nanotechnologies (Raleigh, NC), and Diamond Nanotechnologies (Boston, MA). Tetraethyl orthosilicate (TEOS #333859, 99+%), (3-mercaptopropyl) trimethoxysilane (MPS #175617, 95%), and (3-aminopropyl)trimethoxysilane (APS #281778, 98%) were purchased from Sigma-Aldrich (St. Louis, MO). 2-[Methoxy(polyethyleneoxy)6–9propyl]trimethoxysilane (PEG–PS (*n* = 6–9), #SIM6492.7) and 2-[methoxy-(polyethyleneoxy)9–12propyl]trimethoxysilane (PEG–PS (*n* = 9–12), #SIM6492.7), 3,3,3-trifluoropropyl-trimethoxysilane (FMS) (SIT8372.0), carboxyethylsilanetriol sodium salt in water (CES) (SIC2263.0), (3-glycidyl)trimethoxysilane (SIG5840.0), and 11-azidoundecyltrimethoxysilane (11-AMS) (SIA0795.0) were purchased from Gelest, Inc. (Morrisville, PA).

Aerobic Oxidation and Acid–Base–Acid Treatment of Diamond Nanocrystals

Nanodiamond powders were placed in a ceramic boat, loaded into a tube furnace, left open to the air, and heated to a temperature of 525 °C for 5 h. After cooling to room temperature, oxidized HPHT NDs had a light yellowish tone after the oxidation of dark amorphous carbon. HPHT ND powders were then further oxidized in sequential steps. Oxidized NDs (300 mg) were placed into a 9:1:1 (H₂SO₄:HNO₃:H₂O/(54:6:6 mL)) acid mixture, stirred at 500 rpm, and heated to 80 °C for 24 h with a refluxing column. After 24 h of refluxing, an additional 500 mL of Milli-Q (18.2 MΩ·cm⁻¹) H₂O was then added to the mixture while stirring and cooled by an ice bath. The acid-ND mixture was then transferred to 50 mL conical centrifuge tubes and centrifuged at 5000 relative centrifugal force (RCF) for 30 min. The acidic supernatant was discarded and the rinsing completed three more times. The removal of all acidic ions was confirmed via pH, and purification cycles were stopped when a pH of 7.5–8.0 was reached. The ND solution (300 mg in 5 mL of Milli-Q water) was then placed into 0.1 M NaOH solution (100 mL) at 80 °C and stirred at 500 rpm with a refluxing column for 24 h. The same centrifugation, decantation, and solubilization cycles with Milli-Q H₂O were repeated 3 times, and 500 μL of 1 M KCl (0.2 μm filtered) was added to induce precipitation per 50 mL of solution. The ND powders were placed in a final acid treatment in 1 M HCl at 80 °C (100 mL) with stirring for 24 h with a refluxing column. The purification steps were again repeated with the addition of 1 M NaCl to induce precipitation. The carboxylated HPHT NDs (ND–COOH) were then solubilized in 18.2 MΩ·cm⁻¹ H₂O at a concentration of 1.0 mg/mL and horn sonicated for 10 min at 70% power with 5:2 s on/off cycles. The final ND–COOH is expected to have approximately 7% carboxyls on the surface as described previously.¹⁸

Ultrathin SiO₂ Growth Procedure of ND–COOH

Ten mL of 1.0 mg/mL ND–COOH was concentrated into a pellet via centrifugation at 21,000 RCF for 30 min in 2 mL centrifuge tubes. The purified ND–COOH pellets were concentrated into 1 mL of 18 MW water by consolidating the ND–COOH pellets to a 10 mg/mL solution. The ND pellet (10 mg) was then dispersed into 9.5 mL of 18 MW water and cup-horn-sonicated for 5 min. The ND–COOH sample in 10.5 mL of water, 37.5 mL of ethanol (99.99%), and 300 μL of neat TEOS was added to a 100 mL single neck round-bottom and was cup-horn-sonicated for 2 min at 70% power. The mixture was set stirring at 500 rpm, and 900 μL of 25% NH₄OH was added to initiate the reaction and capped with a septum at 25 °C. The final concentration of TEOS is 27.3 mM for this protocol. The reaction was allowed to proceed for 5–25 min under stirring and then purified via centrifugation. Large SiO₂ aggregates and microparticles were removed via centrifugation of the solution in 50 mL conical tubes for 30 min at 4000 rpm (2,500 RCF). The ND–SiO₂ supernatant was collected and further purified at 21,000 RCF for 20 min, and the pellets were redispersed in ethanol. The ND–SiO₂ pellets were washed in ethanol three times, methanol three times, and 18.2 MΩ water once by centrifugation at 21,000 RCF for 20 min. The ND–SiO₂ samples were dispersed by bath sonication and vortexing between centrifugation and decantation cycles. The final purified product was dispersed in water at 1 mg/mL, freeze-dried with liquid nitrogen, and cryogenically desiccated in a Labconco lyophilizer. The ND–SiO₂ powders were then stored at 5 °C until they were ready for chemical functionalization. Final powder weights ranged from 15 to 30 mg after silica shell growth.

Functionalization of ND–SiO₂ with PEG, Amines, Fluorine, Carboxylic acids, and Azides

1 mg/mL ND–SiO₂ solutions in ethanol were used for surface functionalization protocols. In a typical 9:1 (PEG:Amines) functionalization protocol, 10 mL of 1 mg/mL ND–SiO₂ particles in ethanol, 20 mL of ethanol (200 proof), 1 mL of NH₄OH (25%), 1.44 mL of PEG–PS (9–12 repeating units), 46 μL of APS, and 750 μL of Milli-Q water were added to a 100 mL round-bottom flask with a stir bar. The solution was stirred overnight at 700 rpm for 24 h at 25°. ND–SiO₂ + PEG + NH₂ particles were washed in ethanol three times by centrifugation at 21,000 RCF for 15 min, sonicated, and vortexed between purification cycles. Functionalization with only amines, fluorines, carboxylates, and azides included addition of 460 μL of APS, 505 μL of FMS, 442 μL of CES, and 860 μL of 11-AMS under the above conditions.

As a demonstration of a biological staining protocol, ND–SiO₂ + PEG + NH₂ with nitrogen vacancy centers was used to stain hippocampal cells and imaged with a scanning confocal microscope. Neuron staining images were reproduced with consent of Profs. Dirk Englund and Edward Boyden (Massachusetts Institute of Technology, Cambridge, MA). Hippocampal cell preparation and staining are similar to work by Chang and Boyden in the literature.⁶⁷

TEM and EDS Measurements

High-resolution transmission electron microscopy was carried out at the Molecular Foundry at Lawrence Berkeley National Laboratory on a JEOL 2100-F instrument at an accelerating voltage of 80–200 keV with an Oxford high solid-angle Silicon Drift Detector (SDD) X-ray Energy Dispersive Spectrometer (EDS) system for chemical elemental analysis and a High-Angle Annular Dark Field (HAADF) detector. Samples were deposited from solution onto ultrathin holey carbon TEM grids from Ted Pella (#01824). To render the TEM grids hydrophilic, they were plasma etched in a Hummer 6.2 for 3 min. A single drop from a pasteur pipet was deposited while holding the TEM grids in self-closing tweezers, and the droplet was reduced in volume with a pie-shaped piece of filter paper and allowed to air-dry. Analysis of silica shell thicknesses was performed by using ImageJ software.

DRIFTS Parameters and Analysis

Diffuse reflectance infrared Fourier transmission spectroscopy (DRIFTS) was collected on a Thermo-Nicolet 6700 instrument with a Praying Mantis DRIFTS attachment and the high-temperature reaction chamber. All spectra were collected on a LN₂-cooled MCT detector with 2 cm⁻¹ resolution and 128 scans. All ND samples were mixed with spectroscopic grade KBr for data collection. Samples of 2–3 mg were typically used for DRIFTS collection. Kubelka–Munk transformations were performed individually with linear background corrections using Igor Pro software. Linear backgrounds were generated based on the averaged values of percent reflectance (raw data) in the DRIFTS regions of 2000–2200 and 3800–4000 cm⁻¹. This slope value was then applied to a *y*-intercept function ($y = mx + b$) and applied to spectra for normalized reflectance units (*R*) and then transformed using the Kubelka–Munk equation to make the data proportional to concentration:

$$\text{KM Units} = \frac{(1 - R^2)}{2R} \quad (2)$$

Infrared values were cross-referenced to *Infrared and Raman characteristic group frequencies: tables and charts* by Socrates and HPHT ND studies.^{54,68–71}

ND–OH, ND–COOH, and ND–SiO₂ Deposition on Gold-Coated Silicon Wafers for XAS, XPS, and XES Experimentation

Gold-coated silicon wafers from LGA thin films (Santa Clara, CA) were cut into 1 cm × 1 cm squares, bath-sonicated in acetone, 2-propanol, and 18 MΩ water three times, and dried with a N₂ gun. The wafers were then etched for a minimum of 10 min with a piranha solution (90 mL concentrated sulfuric acid and 10 mL hydrogen peroxide), with the gold layer facing upward in a crystallizing dish. After drying the etched Au wafer with a N₂ gun, 300 μL of 1 mg/mL ND solution was deposited, dried onto the substrate, and covered with a crystallizing dish. Oxidized and silica-coated nanodiamond samples were prepared using 18 MΩ water as a solvent under open-air conditions at 1 mg/mL concentrations. Note: a 10 nm Ti or Cr adhesion layer is used prior to 100 nm gold deposition on Si substrates. Piranha etching did cause pinhole etching of the gold and adhesion layers.

Synchrotron XAS Data Collection, PFY-XAS/XES Analysis, and RIXS Measurements

X-ray absorption spectroscopy (XAS) and resonant inelastic X-ray scattering (RIXS) measurements were performed at beamline 8–2 and 10–1 at the Stanford Synchrotron Radiation Lightsource, SLAC National Accelerator Laboratory using a spot size of <1 mm². Samples were handled in open-air conditions and mounted to an Al sample bar with conductive carbon tape (#16073-4 Ted Pella, Inc. Redding, CA). The samples were transported to the beamline in a sealed polypropylene jar, and a magnetic mounting piece was attached to the sample bar. Samples were introduced into the analysis chamber after the transfer chamber reached 1 × 10⁻⁷ Torr. The analysis chamber pressure was typically 5 × 10⁻⁹ Torr.

At 8–2 and 10–1, carbon, nitrogen, oxygen, and fluorine K-edge XAS was measured in total electron yield (TEY) mode using 42 × 42, 40 × 40, 30 × 30, and 30 × 30 μm slits, respectively. TEY mode probes approximately 5–15 nm of the sample depth in normal conditions, and all experiments were conducted under ultrahigh vacuum conditions (~5 × 10⁻⁹ Torr). After the optics were focused, the reference absorption intensity of the incoming X-ray beam was measured using a sample of gold-coated mesh and used to correct for beam instability. XAS data were collected at an incident electric field vector of 54.7°. For the spectral analysis, the linear pre-edge background was subtracted from the raw XAS spectra. The region used to estimate the background before the absorption edge of carbon, nitrogen, oxygen, and fluorine was 260–280, 370–380, 510–530, and 670–680 eV, respectively. A postedge normalization was also performed in the continuum region at 380 eV for carbon, 420 eV for nitrogen, 580 eV for oxygen, and 730 eV for fluorine using a batch

processing macro in Igor Pro. Energy calibration was performed using the signal from the diamond core-hole exciton which is determined to be 289.0 eV as described elsewhere.³⁸ X-ray energy calibration of the synchrotron light source was performed during grating changes with a Ni slab (Ni L3 absorption) and a 1-point fitting procedure.

Resonant inelastic X-ray scattering (RIXS) measurements were performed using the superconducting transition edge sensor (TES) X-ray detector as described elsewhere by Lee and Titus.^{72,73} The TES allows for background-free X-ray detection with good energy resolution (~1.5 eV) without diffraction grating. An RIXS measurement is performed by sweeping monochromator photon energies across the absorption edge and collecting a time-tagged X-ray pattern across the TES detector. The TES allows for all photons to be simultaneously collected across all detector elements in the array. The RIXS data were integrated to produce partial fluorescence yield (PFY)-XAS and X-ray emission spectroscopy (XES) spectra.

Laboratory XPS Measurements and Analysis

A Thermo Scientific K-Alpha Surface Analysis XPS instrument at the Molecular Foundry was utilized to probe carbon, nitrogen, and bromine signals on the surface of the ND–OH and ND–SiO₂ samples. The K-Alpha XPS has a combined low energy electron and ion flood source and is utilized to suppress charging during all data collection. The XPS X-ray source is an Al Kα microfocused monochromator and is equipped with a 180° double hemispherical analyzer with a 128-channel detector. The low-resolution and high-resolution pass energies are 200.0 and 50.0 eV, respectively. The low-resolution and high-resolution energy step sizes are 1.0 and 0.1 eV, respectively. For high-resolution scans, 50 scans were taken for nitrogen and 10 scans for oxygen, silicon, and carbon with a dwell time of 50 ms to ensure a good signal-to-noise. The electron acceptance angle was 55°, and survey scans were performed over a binding energy range of 0–1350 eV with a pass energy of 200 eV. Three scans were summed, and a dwell time of 10 ms was used.

XPS analysis was performed using Igor Pro software and the CASA-XPS software package, and standard background subtraction and fitting protocols were followed for survey and high-resolution scans. Quantitative analysis of survey scans to determine the atomic % concentrations of individual elements was performed using CASA-XPS software, and Tougaard backgrounds were applied with relative sensitive factor (RSF) values being applied for each element. RSF values for C, O, and Si were 1.0, 2.93, and 0.817, respectively. Atomic % concentrations are calculated using equation:

$$X_A = \frac{(I_A E^\alpha)/(R_A T(E))}{\sum (I_i E^\alpha)/(R_i T(E))} \quad (3)$$

where *X* is the atomic percentage of element *A*, *R_i* is the RSF for the relative intensity *I_i*, and *T(E)* is the transmission function of the instrument for intensity *I_i* at kinetic energy *E*.⁷⁴ The *α* term in the exponent of kinetic energy *E* is used to adjust the analyzer specifications. The VAMAS (Versailles Project on Advanced Materials and Standards) file collected by the K-Alpha instrument allowed for all needed transmission function information to be applied for quantification purposes. The VAMAS file type is ISO 14976 compliant. XPS features from the thin film substrate include Au 4f, Si 2p, and Ti 3s found at 85, 99, and 59 eV, respectively.

SESSA Simulations. The software package Simulation of Electron Spectra for Surface Analysis (SESSA) version 2.2.0, produced by Werner, Smekal, and Powell, was used to simulate the emission of Auger electrons from diamond- and silica-coated diamond samples. The user interface is intuitive and includes the generation of the sample, peak selection, parameter selection, and experimental configuration. The sample generation was done with the layered sphere preset and included a 30 nm diamond core, 0–40 nm of silica, and a Au substrate as the underlayer. The experimental configuration was matched to the photon energy of beamlines 8–2 and 10–1 at SSRL at 289.0 eV that generates the diamond core-hole exciton.^{38,39} Data collection geometry for orientation of the theta values for sample surface normal, orientation of the analyzer axis, orientation of the source axis, and orientation of polarization vector was set to 0° and

ranged from 0° to 90° in increments of 15°, 54°, and 0°, respectively. All phi values were set to 0° in the geometry setting. Peaks of interest included the Auger peaks of C KL1L1 at 246.8 eV, C KL1L23 at 257.4 eV, and C KL23L23 at 268.0 eV and complementary Au 4f, Au 5s, Si 2p, and O 2s photoemission peaks. The carbon diamond core and amorphous SiO₂ shells were assigned a standard band gap and atomic density of 5.5 eV⁷⁵ and 1.17 × 10²³ atoms/cm³ and 9.1 eV⁷⁶ and 6.58 × 10²² atoms/cm³, respectively. The thickness of SiO₂ shells was varied from 0.1 to 30 nm in the SESSA software, and the intensity of the C Auger features was tracked. Screenshots of the SESSA user interface are shown in Figure S1.

Thermogravimetric Analysis–Mass Spectroscopy (TGA–MS) of ND–SiO₂. As prepared ND–SiO₂ samples in ethanol or water were dried on a Si wafer and collected as a powder for TGA–MS characterization. The TGA–MS was carried out on a PerkinElmer TGA–GC–MS system with a TGA 8000, Clarus 680 gas chromatograph, Clarus SQ 8T mass spectrometer, and Transfer Line (TL) 8500 TG–GCMS interface system. The carrier gas was high-purity helium (99.9999% purity). The TGA 8000 experimental conditions included a temperature ramp from 30 to 700 °C at 10 °C/min, a sample purge of 60 mL/min, balance purge of 40 mL/min, and the use of 5 mg of ND–SiO₂ into a tared ceramic sampling pan (Fisher Sci #N5320102). The evolved gas was transferred by the TL 8500 at 270 °C with a flow rate of 70 mL/min into the TG–GCMS. The gas chromatograph (GC) line was bypassed, and the evolved gas was sent into the mass spectrometer (MS). MS data collection included standard conditions of –70 V electron energy, a source temperature of 100 °C, and trap emission of 100 V.

■ ASSOCIATED CONTENT

Supporting Information

The Supporting Information is available free of charge at <https://pubs.acs.org/doi/10.1021/acsnanoscienceau.3c00033>.

Thermogravimetric analysis–mass spectroscopy (TGA–MS) confirming the silica–ND bonding environment, fluorescent scanning confocal images of NV center stained neurons, TEM of silica-coated NDs, X-ray photoelectron spectroscopy data, and resonant inelastic X-ray spectroscopy for C 1s, N 1s, and O 1s edges (PDF)

■ AUTHOR INFORMATION

Corresponding Author

Abraham Wolcott – Department of Chemistry, San José State University, San José, California 95192, United States;
orcid.org/0000-0002-4025-3040;
Email: abraham.wolcott@sjsu.edu

Authors

Perla J. Sandoval – Department of Chemistry, San José State University, San José, California 95192, United States
Karen Lopez – Department of Chemistry, San José State University, San José, California 95192, United States
Andres Arreola – Department of Chemistry, San José State University, San José, California 95192, United States
Anida Len – Department of Chemistry, San José State University, San José, California 95192, United States
Nedah Basravi – Department of Chemistry, San José State University, San José, California 95192, United States
Pomaikaimaikalani Yamaguchi – Department of Chemistry, San José State University, San José, California 95192, United States
Rina Kawamura – Department of Chemistry, San José State University, San José, California 95192, United States

Camron X. Stokes – Department of Chemistry, San José State University, San José, California 95192, United States
Cynthia Melendrez – Department of Chemistry, San José State University, San José, California 95192, United States
David Simpson – Department of Chemistry, San José State University, San José, California 95192, United States
Sang-Jun Lee – Stanford Synchrotron Radiation Lightsource, SLAC National Accelerator Laboratory, Menlo Park, California 94025, United States; orcid.org/0000-0002-8199-3993
Charles James Titus – Department of Physics, Stanford University, Palo Alto, California 94025, United States; orcid.org/0000-0001-6312-8552
Virginia Altoe – The Molecular Foundry, Lawrence Berkeley National Laboratory, Berkeley, California 94720, United States
Sami Sainio – Stanford Synchrotron Radiation Lightsource, SLAC National Accelerator Laboratory, Menlo Park, California 94025, United States; Microelectronics Research Unit, University of Oulu, Oulu 90014, Finland
Dennis Nordlund – Stanford Synchrotron Radiation Lightsource, SLAC National Accelerator Laboratory, Menlo Park, California 94025, United States
Kent Irwin – Stanford Synchrotron Radiation Lightsource, SLAC National Accelerator Laboratory, Menlo Park, California 94025, United States; Department of Physics, Stanford University, Palo Alto, California 94025, United States

Complete contact information is available at:

<https://pubs.acs.org/doi/10.1021/acsnanoscienceau.3c00033>

Author Contributions

#P.J.S., K.L., and A.A. contributed equally. CRediT: **Perla J. Sandoval** data curation, investigation; **Karen Leonor Lopez** data curation, formal analysis, investigation; **Andres Arreola** data curation, investigation; **Anida Len** data curation; **Nedah Basravi** investigation, resources, software, supervision, writing-review & editing; **Pomaikaimaikalani Yamaguchi** data curation, formal analysis; **Rina Kawamura** formal analysis, investigation; **Camron X. Stokes** investigation; **Cynthia Melendrez** formal analysis, investigation; **David Simpson** investigation; **Sang-Jun Lee** data curation, formal analysis, investigation, methodology, writing-review & editing; **Charles James Titus** data curation, formal analysis, investigation; **Virginia Altoe** investigation, resources; **Sami Sainio** investigation; **Dennis Nordlund** formal analysis, resources, software, supervision, writing-review & editing; **Kent Irwin** resources, software, supervision; **Abraham Wolcott** data curation, funding acquisition, methodology, resources, writing-original draft.

Notes

The authors declare no competing financial interest.

■ ACKNOWLEDGMENTS

Abraham Wolcott would like to acknowledge financial support through the National Institutes of Health NIGMS office (1SC3GM125574-01), Army Research Office (W911NF1810453 and W911NF17S000205) through the Department of Defense and the National Science Foundation #2213520. Work at the Molecular Foundry was supported by the Office of Science, Office of Basic Energy Sciences, of the U.S. Department of Energy under Contract No. DE-AC02-

05SCH11231. The TES spectrometer was developed with funding from the Department of Energy, Laboratory Directed Research and Development program under Contract No. DE-AC02-76SF00515. This work was supported by the U.S. Department of Energy Office of Basic Energy Sciences Proposal No. 100487. The use of the Stanford Synchrotron Radiation Lightsource, SLAC National Accelerator Laboratory, is supported by the U.S. Department of Energy, Office of Science, Office of Basic Energy Sciences under Contract No. DE-AC02-76SF00515. Perla Jasmine Sandoval would like to acknowledge support through the MARC and RISE program at SJSU (ST34GM008253-33 and 5R25GM071381-13). Karen Lopez would like to acknowledge support through the RISE program at SJSU (5R25GM071381-13). We would also like to acknowledge William B. Doriese, Galen C. O'Neil, Daniel S. Swetz and Joel N. Ullom, of the Quantum Electromagnetics Division at the National Institutes of Standards and Technology in Boulder, CO. for the engineering, design, manufacturing, and installation of the transition edge sensor at beamline 10-1 at SSRL.

REFERENCES

- (1) Li, L.; Schröder, T.; Chen, E. H.; Walsh, M.; Bayn, I.; Goldstein, J.; Gaathon, O.; Trusheim, M. E.; Lu, M.; Mower, J.; et al. Coherent spin control of a nanocavity-enhanced qubit in diamond. *Nat. Commun.* **2015**, *6* (1), 6173.
- (2) Pfaff, W.; Hensen, B. J.; Bernien, H.; van Dam, S. B.; Blok, M. S.; Taminiau, T. H.; Tiggelman, M. J.; Schouten, R. N.; Markham, M.; Twitchen, D. J.; et al. Unconditional quantum teleportation between distant solid-state quantum bits. *Science* **2014**, *345* (6196), 532–535.
- (3) Wehner, S.; Elkouss, D.; Hanson, R. Quantum internet: A vision for the road ahead. *Science* **2018**, *362* (6412), No. aam9288.
- (4) Dreau, A.; Tchekhovateva, A.; El Mahdaoui, A.; Bonato, C.; Hanson, R. Quantum Frequency Conversion of Single Photons from a Nitrogen-Vacancy Center in Diamond to Telecommunication Wavelengths. *Phys. Rev. Appl.* **2018**, *9* (6), No. 064031.
- (5) Awschalom, D. D.; Hanson, R.; Wrachtrup, J.; Zhou, B. B. Quantum technologies with optically interfaced solid-state spins. *Nat. Photonics* **2018**, *12* (9), 516–527.
- (6) Maze, J. R.; Stanwix, P. L.; Hodges, J. S.; Hong, S.; Taylor, J. M.; Cappellaro, P.; Jiang, L.; Dutt, M. V. G.; Togan, E.; Zibrov, A. S.; et al. Nanoscale magnetic sensing with an individual electronic spin in diamond. *Nature* **2008**, *455* (7213), 644–U641.
- (7) Taylor, J. M.; Cappellaro, P.; Childress, L.; Jiang, L.; Budker, D.; Hemmer, P. R.; Yacoby, A.; Walsworth, R.; Lukin, M. D. High-sensitivity diamond magnetometer with nanoscale resolution. *Nat. Phys.* **2008**, *4* (10), 810–816.
- (8) McGuinness, L. P.; Yan, Y.; Stacey, A.; Simpson, D. A.; Hall, L. T.; Maclaurin, D.; Prawer, S.; Mulvaney, P.; Wrachtrup, J.; Caruso, F.; et al. Quantum measurement and orientation tracking of fluorescent nanodiamonds inside living cells. *Nat. Nanotechnol.* **2011**, *6* (6), 358–363.
- (9) Atature, M.; Englund, D.; Vamivakas, N.; Lee, S. Y.; Wrachtrup, J. Material platforms for spin-based photonic quantum technologies. *Nat. Rev. Mater.* **2018**, *3* (5), 38–51.
- (10) Kucsko, G.; Maurer, P. C.; Yao, N. Y.; Kubo, M.; Noh, H. J.; Lo, P. K.; Park, H.; Lukin, M. D. Nanometre-scale thermometry in a living cell. *Nature* **2013**, *500* (7460), 54–58.
- (11) Tsai, A.; Aghajamali, A.; Dontschuk, N.; Johnson, B. C.; Usman, M.; Schenk, A. K.; Sear, M.; Pakes, C. I.; Hollenberg, L. C. L.; McCallum, J. C.; et al. Epitaxial Formation of SiC on (100) Diamond. *ACS Appl. Electron. Mater.* **2020**, *2* (7), 2003–2009.
- (12) Hiram, K.; Taniyasu, Y.; Kasu, M. AlGaIn/GaN high-electron mobility transistors with low thermal resistance grown on single-crystal diamond (111) substrates by metalorganic vapor-phase epitaxy. *Appl. Phys. Lett.* **2011**, *98* (16), No. 3574531.
- (13) Xie, M. Z.; Yu, X. F.; Rodgers, L. V. H.; Xu, D. H.; Chi-Duran, I.; Toros, A.; Quack, N.; de Leon, N. P.; Maurer, P. C. Biocompatible surface functionalization architecture for a diamond quantum sensor. *Proc. Natl. Acad. Sci. U. S. A.* **2022**, *119* (8), No. e2114186119.
- (14) Rendler, T.; Neburkova, J.; Zemek, O.; Kotek, J.; Zappe, A.; Chu, Z. Q.; Cigler, P.; Wrachtrup, J. Optical imaging of localized chemical events using programmable diamond quantum nanosensors. *Nat. Commun.* **2017**, *8*, 14701.
- (15) Slegerova, J.; Hajek, M.; Rehor, I.; Sedlak, F.; Stursa, J.; Hruby, M.; Cigler, P. Designing the nanobiointerface of fluorescent nanodiamonds: highly selective targeting of glioma cancer cells. *Nanoscale* **2015**, *7* (2), 415–420.
- (16) Rehor, I.; Lee, K. L.; Chen, K.; Hajek, M.; Havlik, J.; Lokajova, J.; Masat, M.; Slegerova, J.; Shukla, S.; Heidari, H.; et al. Plasmonic Nanodiamonds: Targeted Core-Shell Type Nanoparticles for Cancer Cell Thermoablation. *Adv. Healthcare Mater.* **2015**, *4* (3), 460–468.
- (17) Chu, Z.; Zhang, S.; Zhang, B.; Zhang, C.; Fang, C.-Y.; Rehor, I.; Cigler, P.; Chang, H.-C.; Lin, G.; Liu, R.; et al. Unambiguous observation of shape effects on cellular fate of nanoparticles. *Sci. Rep.* **2014**, *4*, 4495. <http://www.nature.com/srep/2014/140328/srep04495/abs/srep04495.html#supplementary-information>
- (18) Nguyen, T. T.-B.; Chang, H.-C.; Wu, V. W.-K. Adsorption and hydrolytic activity of lysozyme on diamond nanocrystallites. *Diamond Relat. Mater.* **2007**, *16* (4), 872–876.
- (19) Gerion, D.; Pinaud, F.; Williams, S. C.; Parak, W. J.; Zanchet, D.; Weiss, S.; Alivisatos, A. P. Synthesis and properties of biocompatible water-soluble silica-coated CdSe/ZnS semiconductor quantum dots. *J. Phys. Chem. B* **2001**, *105* (37), 8861–8871.
- (20) Alivisatos, P. The use of nanocrystals in biological detection. *Nat. Biotechnol.* **2004**, *22* (1), 47–52.
- (21) Ghosh Chaudhuri, R.; Paria, S. Core/Shell Nanoparticles: Classes, Properties, Synthesis Mechanisms, Characterization, and Applications. *Chem. Rev.* **2012**, *112* (4), 2373–2433.
- (22) Lee, J. R. I.; Whitley, H. D.; Meulenberg, R. W.; Wolcott, A.; Zhang, J. Z.; Prendergast, D.; Lovingood, D. D.; Strouse, G. F.; Ogitsu, T.; Schwegler, E.; et al. Ligand-Mediated Modification of the Electronic Structure of CdSe Quantum Dots. *Nano Lett.* **2012**, *12* (6), 2763–2767.
- (23) Meulenberg, R. W.; Lee, J. R. I.; Wolcott, A.; Zhang, J. Z.; Terminello, L. J.; van Buuren, T. Determination of the Excitation Binding Energy in CdSe Quantum Dots. *ACS Nano* **2009**, *3* (2), 325–330.
- (24) Wei, H.; Zhou, J.; Zhang, L.; Wang, F.; Wang, J.; Jin, C. The Core/Shell Structure of CdSe/ZnS Quantum Dots Characterized by X-Ray Absorption Fine Spectroscopy. *J. Nanomater.* **2015**, *2015*, No. 764712.
- (25) Carpenter, E. E.; Calvin, S.; Stroud, R. M.; Harris, V. G. Passivated Iron as Core-Shell Nanoparticles. *Chem. Mater.* **2003**, *15* (17), 3245–3246.
- (26) Carroll, K. J.; Hudgins, D. M.; Spurgeon, S.; Kemner, K. M.; Mishra, B.; Boyanov, M. I.; Brown, L. W.; Taheri, M. L.; Carpenter, E. E. One-Pot Aqueous Synthesis of Fe and Ag Core/Shell Nanoparticles. *Chem. Mater.* **2010**, *22* (23), 6291–6296.
- (27) Zhang, X.; Han, S.; Zhu, B.; Zhang, G.; Li, X.; Gao, Y.; Wu, Z.; Yang, B.; Liu, Y.; Baaziz, W.; et al. Reversible loss of core-shell structure for Ni-Au bimetallic nanoparticles during CO₂ hydrogenation. *Nat. Catal.* **2020**, *3* (4), 411–417.
- (28) Signorini, L.; Pasquini, L.; Savini, L.; Carboni, R.; Boscherini, F.; Bonetti, E.; Giglia, A.; Pedio, M.; Mahne, N.; Nannarone, S. Size-dependent oxidation in iron/iron oxide core-shell nanoparticles. *Phys. Rev. B* **2003**, *68* (19), No. 195423.
- (29) Alayoglu, S.; Zavalij, P.; Eichhorn, B.; Wang, Q.; Frenkel, A. I.; Chupas, P. Structural and Architectural Evaluation of Bimetallic Nanoparticles: A Case Study of Pt-Ru Core-Shell and Alloy Nanoparticles. *ACS Nano* **2009**, *3* (10), 3127–3137.
- (30) Park, J.-I.; Kim, M. G.; Jun, Y.-W.; Lee, J. S.; Lee, W.-R.; Cheon, J. Characterization of Superparamagnetic “Core-Shell” Nanoparticles and Monitoring Their Anisotropic Phase Transition to Ferromagnetic

- "Solid Solution" Nanoalloys. *J. Am. Chem. Soc.* **2004**, *126* (29), 9072–9078.
- (31) Lee, W.-R.; Kim, M. G.; Choi, J.-R.; Park, J.-I.; Ko, S. J.; Oh, S. J.; Cheon, J. Redox–Transmetalation Process as a Generalized Synthetic Strategy for Core–Shell Magnetic Nanoparticles. *J. Am. Chem. Soc.* **2005**, *127* (46), 16090–16097.
- (32) Foucher, A. C.; Yang, S.; Rosen, D. J.; Lee, J. D.; Huang, R.; Jiang, Z.; Barrera, F. G.; Chen, K.; Hollyer, G. G.; Friend, C. M.; et al. Synthesis and Characterization of Core-Shell Cu-Ru, Cu-Rh, and Cu-Ir Nanoparticles. *J. Am. Chem. Soc.* **2022**, *144* (17), 7919–7928.
- (33) Rehor, I.; Slegerova, J.; Kucka, J.; Proks, V.; Petrakova, V.; Adam, M. P.; Treussart, F.; Turner, S.; Bals, S.; Sacha, P.; et al. Fluorescent Nanodiamonds Embedded in Biocompatible Translucent Shells. *Small* **2014**, *10* (6), 1106–1115.
- (34) Rehor, I.; Mackova, H.; Filippov, S. K.; Kucka, J.; Proks, V.; Slegerova, J.; Turner, S.; Van Tendeloo, G.; Ledvina, M.; Hruby, M.; et al. Fluorescent Nanodiamonds with Bioorthogonally Reactive Protein-Resistant Polymeric Coatings. *ChemPlusChem* **2014**, *79* (1), 21–24.
- (35) Schiros, T.; Nordlund, D.; Palova, L.; Prezzi, D.; Zhao, L. Y.; Kim, K. S.; Wurstbauer, U.; Gutierrez, C.; Delongchamp, D.; Jaye, C.; et al. Connecting Dopant Bond Type with Electronic Structure in N-Doped Graphene. *Nano Lett.* **2012**, *12* (8), 4025–4031.
- (36) Raty, J. Y.; Galli, G.; Bostedt, C.; van Buuren, T. W.; Terminello, L. J. Quantum confinement and fullerene-like surface reconstructions in nanodiamonds. *Phys. Rev. Lett.* **2003**, *90* (3), No. 037401.
- (37) Chang, Y. K.; Hsieh, H. H.; Pong, W. F.; Tsai, M. H.; Chien, F. Z.; Tseng, P. K.; Chen, L. C.; Wang, T. Y.; Chen, K. H.; Bhusari, D. M.; et al. Quantum Confinement Effect in Diamond Nanocrystals Studied by X-Ray-Absorption Spectroscopy. *Phys. Rev. Lett.* **1999**, *82* (26), 5377–5380.
- (38) Morar, J. F.; Himpel, F. J.; Hollinger, G.; Hughes, G.; Jordan, J. L. OBSERVATION OF A C-1S CORE EXCITON IN DIAMOND. *Phys. Rev. Lett.* **1985**, *54* (17), 1960–1963.
- (39) Wolcott, A.; Schiros, T.; Trusheim, M. E.; Chen, E. H.; Nordlund, D.; Diaz, R. E.; Gaathon, O.; Englund, D.; Owen, J. S. Surface structure of aerobically oxidized diamond nanocrystals. *J. Phys. Chem. C* **2014**, *118* (46), 26695–26702.
- (40) Henke, B. L.; Liesegang, J.; Smith, S. D. SOFT-X-RAY-INDUCED SECONDARY-ELECTRON EMISSION FROM SEMI-CONDUCTORS AND INSULATORS - MODELS AND MEASUREMENTS. *Phys. Rev. B* **1979**, *19* (6), 3004–3021.
- (41) Henke, B. L.; Smith, J. A.; Attwood, D. T. 0.1–10-KEV X-RAY-INDUCED ELECTRON EMISSIONS FROM SOLIDS - MODELS AND SECONDARY-ELECTRON MEASUREMENTS. *J. Appl. Phys.* **1977**, *48* (5), 1852–1866.
- (42) Maurer, P. C.; Kucsko, G.; Latta, C.; Jiang, L.; Yao, N. Y.; Bennett, S. D.; Pastawski, F.; Hunger, D.; Chisholm, N.; Markham, M.; et al. Room-Temperature Quantum Bit Memory Exceeding One Second. *Science* **2012**, *336* (6086), 1283–1286.
- (43) Jones, R. G.; Woodruff, D. P. Sampling depths in total yield and reflectivity SEXAFS studies in the soft X-ray region. *Surf. Sci.* **1982**, *114* (1), 38–46.
- (44) Stöhr, J. *NEXAFS Spectroscopy*; Springer-Verlag: Berlin Heidelberg, 1992.
- (45) Kasrai, M.; Lennard, W. N.; Brunner, R. W.; Bancroft, G. M.; Bardwell, J. A.; Tan, K. H. Sampling depth of total electron and fluorescence measurements in Si L- and K-edge absorption spectroscopy. *Appl. Surf. Sci.* **1996**, *99* (4), 303–312.
- (46) Ziaja, B.; van der Spoel, D.; Szöke, A.; Hajdu, J. Auger-electron cascades in diamond and amorphous carbon. *Phys. Rev. B* **2001**, *64* (21), No. 214104.
- (47) Neburkova, J.; Vavra, J.; Cigler, P. Coating nanodiamonds with biocompatible shells for applications in biology and medicine. *Curr. Opin. Solid State Mater. Sci.* **2017**, *21* (1), 43–53.
- (48) Harris, M. T.; Brunson, R. R.; Byers, C. H. THE BASE-CATALYZED-HYDROLYSIS AND CONDENSATION-REACTIONS OF DILUTE AND CONCENTRATED TEOS SOLUTIONS. *J. Non-Cryst. Solids* **1990**, *121* (1–3), 397–403.
- (49) Chuit, C.; Corriu, R. J. P.; Reye, C.; Young, J. C. Reactivity of penta- and hexacoordinate silicon compounds and their role as reaction intermediates. *Chem. Rev.* **1993**, *93* (4), 1371–1448.
- (50) Delak, K. M.; Sahai, N. Amine-Catalyzed Biomimetic Hydrolysis and Condensation of Organosilicate. *Chem. Mater.* **2005**, *17* (12), 3221–3227.
- (51) Delak, K. M.; Sahai, N. Mechanisms of Amine-Catalyzed Organosilicate Hydrolysis at Circum-Neutral pH. *J. Phys. Chem. B* **2006**, *110* (36), 17819–17829.
- (52) Stöber, W.; Fink, A.; Bohn, E. Controlled growth of monodisperse silica spheres in the micron size range. *J. Colloid Interface Sci.* **1968**, *26* (1), 62.
- (53) Pandey, K. C. NEW DIMERIZED-CHAIN MODEL FOR THE RECONSTRUCTION OF THE DIAMOND (111)-(2 × 1) SURFACE. *Phys. Rev. B* **1982**, *25* (6), 4338–4341.
- (54) Osswald, S.; Yushin, G.; Mochalin, V.; Kucheyev, S. O.; Gogotsi, Y. Control of sp(2)/sp(3) carbon ratio and surface chemistry of nanodiamond powders by selective oxidation in air. *J. Am. Chem. Soc.* **2006**, *128* (35), 11635–11642.
- (55) Frazer, B. H.; Gilbert, B.; Sonderegger, B. R.; De Stasio, G. The probing depth of total electron yield in the sub-keV range: TEY-XAS and X-PEEM. *Surf. Sci.* **2003**, *537* (1–3), 161–167.
- (56) Smekal, W.; Werner, W. S. M.; Powell, C. J. Simulation of electron spectra for surface analysis (SESSA): a novel software tool for quantitative Auger-electron spectroscopy and X-ray photoelectron spectroscopy. *Surf. Interface Anal.* **2005**, *37* (11), 1059–1067.
- (57) Outka, D. A.; Stöhr, J.; Madix, R. J.; Rotermund, H. H.; Hermesmeier, B.; Solomon, J. NEXAFS STUDIES OF COMPLEX ALCOHOLS AND CARBOXYLIC-ACIDS ON THE SI(111)(7 × 7) SURFACE. *Surf. Sci.* **1987**, *185* (1–2), 53–74.
- (58) Santoro, M.; Gorelli, F.; Haines, J.; Cambon, O.; Levelut, C.; Garbarino, G. Silicon carbonate phase formed from carbon dioxide and silica under pressure. *Proc. Natl. Acad. Sci. U. S. A.* **2011**, *108* (19), 7689–7692. From NLM
- (59) Leinweber, P.; Kruse, J.; Walley, F. L.; Gillespie, A.; Eckhardt, K.-U.; Blyth, R. I. R.; Regier, T. Nitrogen K-edge XANES - an overview of reference compounds used to identify 'unknown' organic nitrogen in environmental samples. *J. Synchrotron Radiat.* **2007**, *14* (6), 500–511.
- (60) Melendrez, C.; Lopez-Rosas, J. A.; Stokes, C. X.; Cheung, T. C.; Lee, S.-J.; Titus, C. J.; Valenzuela, J.; Jeanpierre, G.; Muhammad, H.; Tran, P.; et al. Metastable Brominated Nanodiamond Surface Enables Room Temperature and Catalysis-Free Amine Chemistry. *J. Phys. Chem. Lett.* **2022**, *13*, 1147–1158.
- (61) Darlatt, E.; Traulsen, C. H. H.; Poppenberg, J.; Richter, S.; Kuhn, J.; Schalley, C. A.; Unger, W. E. S. Evidence of click and coordination reactions on a self-assembled monolayer by synchrotron radiation based XPS and NEXAFS. *J. Electron Spectrosc. Relat. Phenom.* **2012**, *185* (3–4), 85–89.
- (62) Darlatt, E.; Nefedov, A.; Traulsen, C. H. H.; Poppenberg, J.; Richter, S.; Dietrich, P. M.; Lippitz, A.; Illgen, R.; Kuhn, J.; Schalley, C. A.; et al. Interpretation of experimental N K NEXAFS of azide, 1,2,3-triazole and terpyridyl groups by DFT spectrum simulations. *J. Electron Spectrosc. Relat. Phenom.* **2012**, *185* (12), 621–624.
- (63) Pauling, L.; Brockway, L. O. The Adjacent Charge Rule and the Structure of Methyl Azide, Methyl Nitrate, and Fluorine Nitrate. *J. Am. Chem. Soc.* **1937**, *59* (1), 13–20.
- (64) Castner, D. G.; Lewis, K. B.; Fischer, D. A.; Ratner, B. D.; Gland, J. L. DETERMINATION OF SURFACE-STRUCTURE AND ORIENTATION OF POLYMERIZED TETRAFLUOROETHYLENE FILMS BY NEAR-EDGE X-RAY ABSORPTION FINE-STRUCTURE, X-RAY PHOTOELECTRON-SPECTROSCOPY, AND STATIC SECONDARY ION MASS-SPECTROMETRY. *Langmuir* **1993**, *9* (2), 537–542.
- (65) Brassard, J.-D.; Sarkar, D. K.; Perron, J. Synthesis of Monodisperse Fluorinated Silica Nanoparticles and Their Super-

hydrophobic Thin Films. *ACS Appl. Mater. Interfaces* **2011**, *3* (9), 3583–3588.

(66) Kobayashi, K.; Wei, J.; Iida, R.; Ijiro, K.; Niikura, K. Surface engineering of nanoparticles for therapeutic applications. *Polym. J.* **2014**, *46* (8), 460–468.

(67) Chang, J.-B.; Chen, F.; Yoon, Y.-G.; Jung, E. E.; Babcock, H.; Kang, J. S.; Asano, S.; Suk, H.-J.; Pak, N.; Tillberg, P. W.; et al. Iterative expansion microscopy. *Nat. Methods* **2017**, *14* (6), 593–599.

(68) Socrates, G. *Infrared and Raman characteristic group frequencies: tables and charts*; John Wiley and Sons, 2001.

(69) Krueger, A.; Lang, D. Functionality is Key: Recent Progress in the Surface Modification of Nanodiamond. *Adv. Funct. Mater.* **2012**, *22* (5), 890–906.

(70) Krueger, A.; Stegk, J.; Liang, Y.; Lu, L.; Jarre, G. Biotinylated nanodiamond: Simple and efficient functionalization of detonation diamond. *Langmuir* **2008**, *24* (8), 4200–4204.

(71) Girard, H. A.; Petit, T.; Perruchas, S.; Gacoin, T.; Gesset, C.; Arnault, J. C.; Bergonzo, P. Surface properties of hydrogenated nanodiamonds: a chemical investigation. *Phys. Chem. Chem. Phys.* **2011**, *13* (24), 11517–11523.

(72) Lee, S. J.; Titus, C. J.; Mori, R. A.; Baker, M. L.; Bennett, D. A.; Cho, H. M.; Doriese, W. B.; Fowler, J. W.; Gaffney, K. J.; Gallo, A.; et al. Soft X-ray spectroscopy with transition-edge sensors at Stanford Synchrotron Radiation Lightsource beamline 10–1. *Rev. Sci. Instrum.* **2019**, *90* (11), 113101.

(73) Lee, S. J.; Mori, R.; Alpert, B.; Baker, M.; Berry, J.; Cho, H.-M.; Denison, E.; Doriese, W.; Fowler, J.; Gaffney, K. Ultrasensitive probing of the local electronic structure of nitrogen doped carbon and its applications to 2D electronics, catalysis and bio-physics. In *ABSTRACTS OF PAPERS OF THE AMERICAN CHEMICAL SOCIETY*; AMER CHEMICAL SOC: 1155 16TH ST, NW, WASHINGTON, DC 20036 USA; Vol. 253, 2017.

(74) CasaXPS. *CasaXPS User's Manual*, 2001.

(75) Saslow, W.; Bergstresser, T. K.; Cohen, M. L. Band Structure and Optical Properties of Diamond. *Phys. Rev. Lett.* **1966**, *16* (9), 354–356.

(76) Astašauskas, V.; Bellissimo, A.; Kuksa, P.; Tomastik, C.; Kalbe, H.; Werner, W. S. M. Optical and electronic properties of amorphous silicon dioxide by single and double electron spectroscopy. *J. Electron Spectrosc. Relat. Phenom.* **2020**, *241*, 146829.